https://doi.org/10.2352/ISSN.2470-1173.2018.13.IPAS-306

Methods and tools for denoising of complex-valued images based on block-matching and high order singular value decomposition

Mykola Ponomarenko, Vladimir Katkovnik, Karen Egiazarian
Tampere University of Technology, FIN 33101, Tampere, Finland

Abstract

Noise suppression in complex-valued data is an important task for a wide class of applications, in particular concerning the phase retrieval in coherent imaging. The approaches based on BM3D techniques are ones of the most successful in the field. In this paper, we propose and develop a new class of BM3D-style algorithms, which use high order (3D and 4D) singular value decomposition (HOSVD) for transform design in complex domain. This set of the novel algorithms is implemented as a toolbox In Matlab. This development is produced for various types of the complex-domain sparsity: directly in complex domain, real/imaginary and phase/ amplitude parts of complex-valued variables. The group-wise transform design is combined with the different kinds of thresholding including multivariable Wiener filtering. The toolbox includes iterative and non-iterative novel complex-domain algorithms (filters). The efficiency of the developed algorithms is demonstrated on denoising problems with an additive Gaussian complex-valued noise. A special set of the complex-valued test-images was developed with spatially varying correlated phase and amplitudes imitating data typical for optical interferometry and holography. It is shown that for this class of the test-images the developed algorithms demonstrate the state-of-the-art performance.

Keywords: Block matching, Complex domain, Image denoising, Phase imaging, Sparsity, Higher-order singular value decomposition

Introduction

Complex-valued denoising is a reconstruction of complex-valued image $u_o(x)$, its amplitude $a(x)$, phase $\varphi(x)$ and maybe absolute phase $\varphi_{abs}(x)$ from the observed noisy complex-valued data $z : X \to C$, where $X \subset Z^2$ is $2D$ grid of size $\sqrt{n} \times \sqrt{n}$, are modeled as

$$z(x) = u_o(x) + \varepsilon(x), \qquad (1)$$
$$u_o(x) = a(x)e^{j\varphi(x)},$$

where $x \in X$, $u_o(x) \subset \mathbb{C}^{\sqrt{n}\times\sqrt{n}}$ is a clear complex-valued image, and $\varepsilon(x) = \varepsilon_I(x) + j\varepsilon_Q(x) \subset \mathbb{C}^{\sqrt{n}\times\sqrt{n}}$ is complex-valued zero-mean Gaussian circular white noise of variance σ^2 (i.e., ε_I and ε_Q are zero-mean independent Gaussian random variables with variance $\sigma^2/2$).

The following methods are typically used for denoising in the complex domain: point-wise (pixel-wise) nonparametric estimation [1], parametric series (approximations), e.g. windowed Fourier transforms [2], as well as the methods based on sparsity and group-wise sparsity are used. The last sparsity methods based on the BM3D technique [3] mainly provides a better accuracy as compared with counterparts. However, the real-valued transforms used in the conventional BM3D such as wavelets and DST do not suit for processing of complex-valued images.

There are two straightforward ideas to approach the complex-domain problem. First, separate denoising of real and imaginary or phase and amplitude components of complex-valued data by the conventional BM3D applied to the real-valued variables. The drawback of the approach is that usual correlations between real and imaginary components or phase and amplitude are not taken into accounting. The second more productive approach is based on joint consideration of the all parts of the complex-valued variables, in particular, including the correlation of their real and imaginary parts and amplitude and phase.

This paper is devoted to this second group of methods and presents a generalization of the techniques considered in [4], [5],[6]. Our approach essentially uses Singular Value Decomposition (SVD) and High Order Singular Value Decomposition (HOSVD) which allow to decorrelate effectively complex-valued 3D or 4D blocks before noise suppression by thresholding or Wiener filtering. In the paper, new iterative complex-valued image denoising algorithms based on HOSVD are proposed. The toolbox allows a flexible switch between different algorithms and tuning their structure and parameters.

Image denoising:block-matching and HOSVD

The generalized flow chart of the proposed algorithms, in particular, illustrating the used block-matchings is shown on Figure 1.

The following basic steps are used for the algorithm design (details can be seen [6]):

1) Image partitioning into small overlapping rectangular patches (8x8 pixel for the paper);

2) Matching similar patches in 3D/4D groups;

3) 3D/4D HOSVD transform design for decorrelation data in groups;

4) Thresholding and Wiener filtering of transformed group-wise data;

5) Aggregation of the group-wise filtered data in the final estimate.

In the paper we use the transforms generated by HOSVD (TUCKER3) [7] for compact representation of 3D/4D groups.

HOSVD allows to represent the group-wise data (tensor) in the form

$$u^r = \mathbf{S}^r \times_1 \mathbf{T}_{1,r} \times_2 \mathbf{T}_{2,r} \times_3 \mathbf{T}_{3,r}, \qquad (2)$$

where $\mathbf{T}_{1,r} \subset \mathbb{C}^{N_1\times N_1}$, $\mathbf{T}_{2,r} \subset \mathbb{C}^{N_2\times N_2}$ and $T_{3,r} \subset \mathbb{C}^{N_{J_r}\times N_{J_r}}$ are orthonormal transform matrices, $\mathbf{S}^r \in \mathbb{C}^{N_1\times N_2\times J_r}$ is the so-called

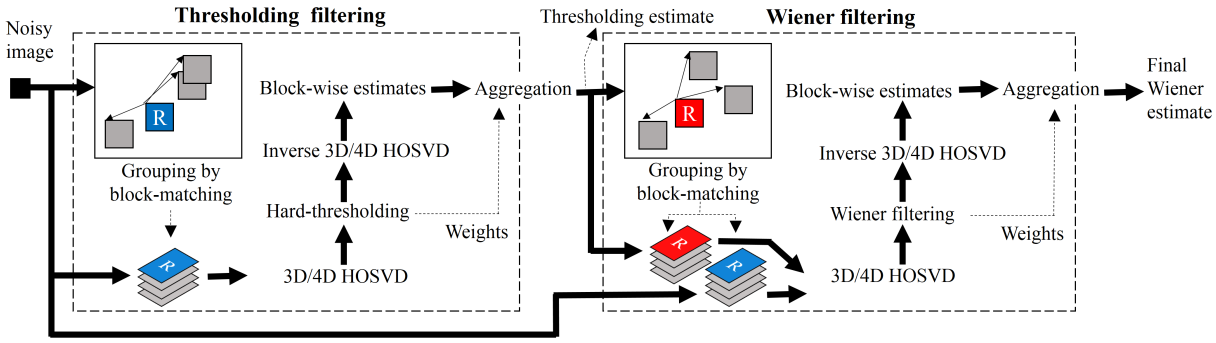

Figure 1. *Flow chart of complex domain BM3D filter.*

core tensor, and symbols $\times_1$, $\times_2$, $\times_3$ stand for the products of the corresponding modes (variables). The matrix transform $\mathbf{T}_{1,r}$ acts with respect to the variable l_1 in the tensor provided that l_2 and l_3 are fixed, similar meaning have the mode transforms $\times_2\mathbf{T}_{2,r}$ and $\times\mathbf{T}_{3,r}$ with respect to the variables l_2 and l_3.

The formula (2) defines the signal through its spectrum (core tensor). The analysis transform can be represented as follows

$$\mathbf{S}^r = u_z^r \times_1 \mathbf{T}_{1,r}^H \times_2 \mathbf{T}_{2,r}^H \times_3 \mathbf{T}_{3,r}^H, \tag{3}$$

where $'H'$ stands for the Hermitian transpose.

Matlab toolbox

The developed algorithms are implemented in MATLAB and constitute Complex Domain Image Denoising (CDID) Toolbox.

The structure of the proposed toolbox for complex-valued images denoising based on HOSVD is shown in Figure 2. A noisy complex-valued image as well as the standard deviation of the white additive complex-valued Gaussian noise are required inputs for any processing in the toolbox.

The CDID toolbox allows to switch between analysis in complex and real domains, use 3D/4D HOSVD, soft/hard thresholding and Wiener filtering, to use PUMA script [8] for phase unwrapping. The toolbox may be applied for a flexible development of more sophisticated denoising algorithms. One example of such algorithm is Wiener filtering followed by the hard thresholding or the iterative scheme described in the next section.

The CDID toolbox also includes the script for generation of reference and noisy test-images with given characteristics (see Figure 3).

These test-images well correspond to real experimental data in following peculiarities:

- higher amplitudes usually correspond to lower phase values and vice versa;

- probability of abrupt changes in phase increases for areas where amplitudes are close to zero;

- object features presented in phase may be absent in amplitude and vice versa.

Iterative algorithms

We propose a set of the novel iterative algorithms built using the discussed above non-iterative algorithms as core elements. These iterative algorithms have the structure derived in [5] from the variational formulation of the problem and shown in Table 1, where CDF (complex domain filter) is any from the non-iterative algorithms and α_t, $\delta_t >$ are the parameters of iterations.

Table 1. Iterative CDF algorithms

	Input: $z \in \mathbb{C}^{\sqrt{n}\times\sqrt{n}}$ (noisy data)
	Parameters: K (iteration number), $\delta > 0$ (thresholding),
	$\alpha > 0$ (regularization).
	Initialization: $u^0 = z$;
	Output: $\hat{u} \in \mathbb{C}^{\sqrt{n}\times\sqrt{n}}$;
1:	for $t = 1, .., K$
2:	$v^t = u^{t-1} + \alpha_{t-1}(z - u^{t-1})$;
3:	$u^t = CDF(v^t, \delta_{t-1})$;
4:	*end*
	$\hat{u} = u^K$.

The thorough optimization of these iterative algorithms results in the three-step iterations with the parameters α_{t-1} and δ_{t-1} varying from step-to-step.

The CDFs with thresholding are used in this optimization without Wiener filtering.

As a result of our analysis the following values are obtained for the parameters of the algorithms: δ_0=0.9, δ_1=0.5, δ_2=0.4, α_0=1, α_1=0.35, α_2=0.25.

Comparative analysis

In this section we present simulation results illustrating and comparing the performance of the developed algorithms.

Noise modeling

Following to [6], the standard deviation of the additive complex-valued noise is calculated according to the formula

$$\sigma = \sigma_{\varphi_z} \cdot mean_x(a_o(x))\sqrt{2}, \tag{4}$$

where $mean_x(a_o(x))$ is the mean value of the amplitude and σ_{φ_z} is the standard deviation of the noise in the phase [1]. This noise standard deviation scaling by the mean amplitude value is introduced in order to control the level of the noise in observations through the noise level in the phase as the phase in the variable of the main interest in this paper. This scaling makes comparable the results for the experiments with different images.

[1] Note, that the factor $\sqrt{2}$ is lost in [6].

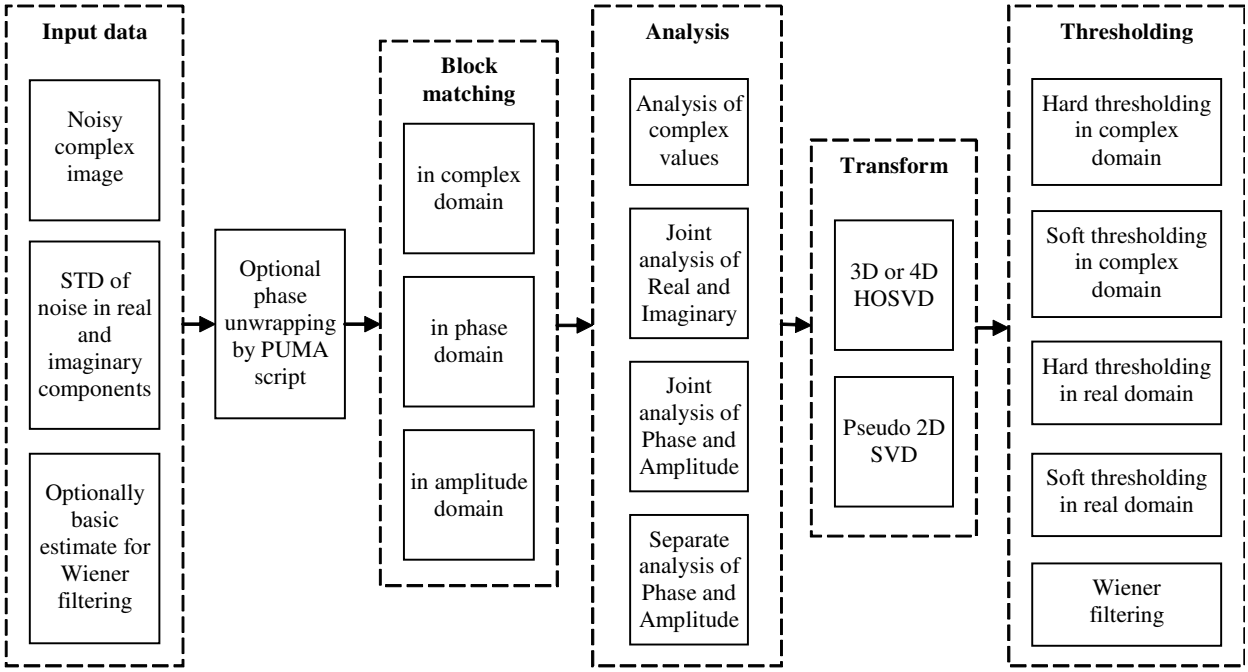

Figure 2. *Structure of the introduced family of the complex domain filters*

The experiments are produced for the following set of the phase standard deviations $\sigma_{\varphi_z} = \{0.05, 0.1, 0.2, 0.3, 0.5, 0.9\}$. The largest σ_{φ_z} corresponds to the very noisy observations.

It can be proved by linearization of $z(x) = a_z(x)\exp(i\varphi_z(x))$ produced for small σ, i.e. for small random components in $a_z(x)$ and $\varphi_z(x)$, that the expectations and variances of amplitude and phase of the observed $z(x)$ are such that

$$E\{a_z(x)\} \simeq a_o(x),\ \sigma^2_{a_z}(x) = var(a_z(x)) \simeq \sigma^2/2, \qquad (5)$$
$$E\{\varphi_z(x)\} \simeq \varphi_o(x),\ \sigma^2_{\varphi_z}(x) = var(\varphi_z(x)) \simeq \sigma^2/(2a^2_o(x)).$$

It proves that experiments with varying σ^2 calculated according to (4) approximately allow to control the noise level in the phase $\sigma^2_{\varphi_z}$.

Accuracy criteria

The following performance criteria are used in the paper for evaluation of the reconstruction accuracy for the complex-valued signals. For the interferometric phase, it is the peak signal-to-noise ratio (*PSNR*):

$$PSNR_{\varphi} = 10\log_{10}\frac{n(2\pi)^2}{||\mathscr{W}(\hat{\varphi}_o - \varphi_o)||_2^2}[dB], \qquad (6)$$

where $\hat{\varphi}_o$ and φ_o are the phase reconstruction and the true phase, respectively; n is the image size in pixels; the phase wrapping operator $\mathscr{W}$ is used in order to eliminate the phase shifts in errors multiple to 2π [9]. The factor $(2\pi)^2$ in the numerator of (6) stays for the squared maximum value of the interferometric phase.

We unwrap the estimated interferometric phase with the PUMA algorithm [8] in order to get estimates of the true absolute phase $\varphi_{o,abs}$. The accuracy of the absolute phase reconstruction is measured by signal-to-noise ratio (SNR) for absolute phase calculated as

$$SNR_{\varphi_{abs}} = 10\log_{10}\frac{||\varphi_{o,abs} - \bar{\varphi}_{o,abs}||_2^2}{||\varphi_{o,abs} - \hat{\varphi}_{o,abs} + \Delta_{\varphi}||_2^2}[dB] \qquad (7)$$

where a scalar Δ_{φ} compensates an invariant shift in the absolute phase estimation multiple to 2π which can appear due to the unwrapping procedure. It is calculated as

$$\Delta_{\varphi} = 2\pi\left[\frac{\overline{\hat{\varphi}}_{0,abs} - \overline{\varphi}_{0,abs}}{2\pi}\right]$$

Here $[\cdot]$ stands for the integer part of the argument and the hat $'-'$means the mean value of the variables.

For the comparative analysis we use the state-of-the-art algorithms for complex-valued images: WFT [10],[2], SpInPhase [9], and SPAR [11], [12], [13].

Compared algorithms

We wish to compare seven algorithms shown in Table 2 for the set of the test-images from Fig. 3 with various levels of the additive noise in observations.

Here ImRe-BM3D HT, ImRe-BM3D WT, ImRe-BM3D IT and CD-BM3D IT are the algorithms implemented using the CDID Toolbox. Both ImRe-BM3D and CD-BM3D are designed using the iterative scheme proposed in the paper. These algorithms are applied with the hard-thresholding and no Wiener filtering.

Numerical analysis

In our tests we use the six phase images shown in Fig. 3 : Lena, Cameraman, Peppers, Pattern, Truncated Gauss and Hills. We consider two cases: interferometric and absolute phase.

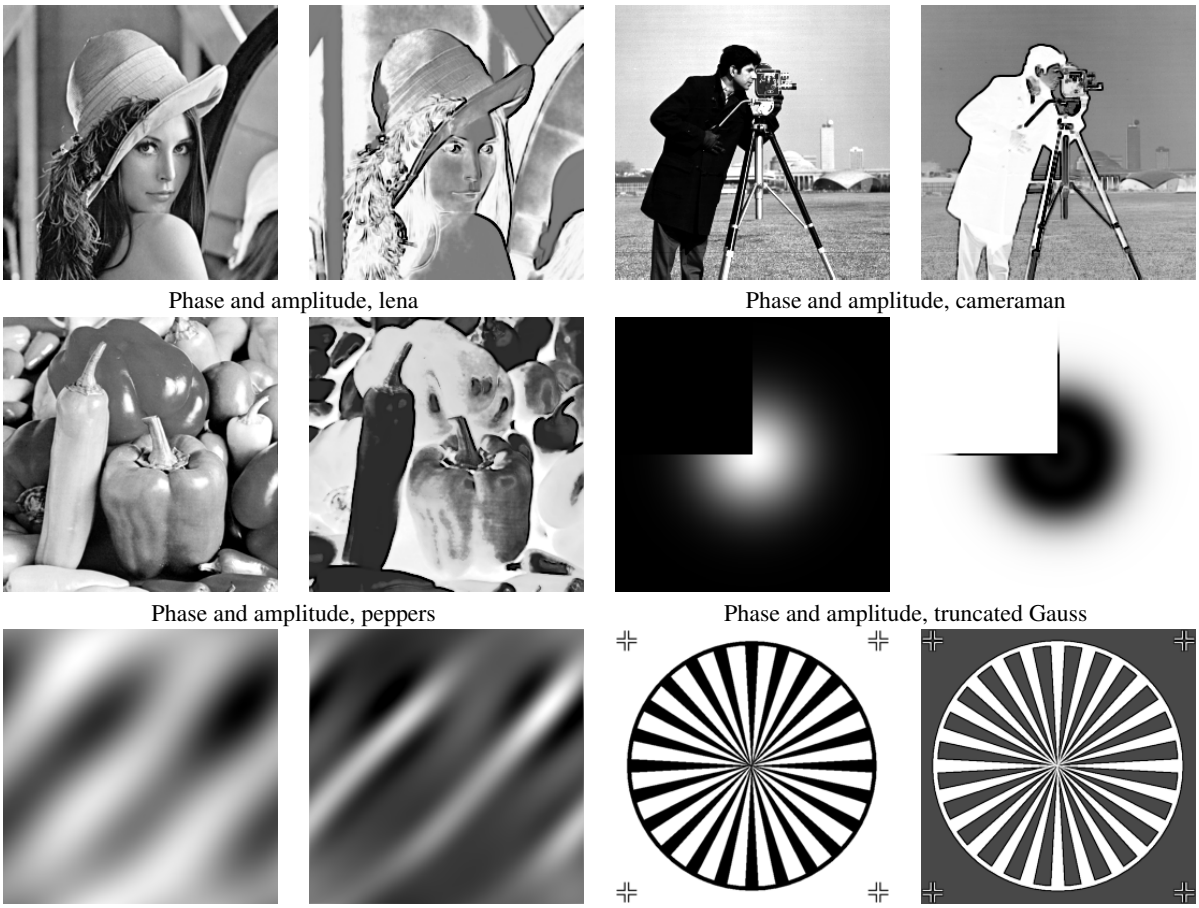

Phase and amplitude, lena | Phase and amplitude, cameraman

Phase and amplitude, peppers | Phase and amplitude, truncated Gauss

Phase and amplitude, hills | Phase and amplitude, patterns

Figure 3. *Complex domain test-images*

Table 2. Compared algorithms

#	Algorithm	Abbreviation
1	ImRe-BM3D with hard-thresholding	ImRe-BM3D HT
2	ImRe-BM3D with hard-thresholding and Wiener filtering	ImRe-BM3D WI
3	Iterative ImRe-BM3D	ImRe-BM3D IT
4	Iterative CD-BM3D	CD-BM3D IT
5	Windowed Fourier Transform	WFT
6	Sparse learning dictionary	SpInPhase
7	Iterative Sparse Phase and Amplitude Retrieval	SPAR

Let $PSNR_{\varphi}(k,l,m)$ be a set of $PSNR_{\varphi}$ calculated for $k \in K$, $l \in L$, $m \in M$, where K, L and M denote the sets of the algorithms, the noise standard deviations (six different values), and six test-images, respectively.

The best algorithm for each test image and for each noise standard deviation is defined as

$$mPSNR_{\varphi}(l,m) = \max_{K} PSNR_{\varphi}(k,l,m). \quad (8)$$

We compare the algorithms with this best result using the differences between the corresponding PSNRs:

$$\Delta PSNR_{\varphi}(k,l,m) = PSNR_{\varphi}(k,l,m) - mPSNR_{\varphi}(l,m). \quad (9)$$

The box-plots on the Figure 4 being depicted for each algorithm (each k) give comparative statistics with respect to two other indices l and m, i.e. for test-images and for noise standard deviations. The upper and lower edges of the rectangle boxes correspond to 25% and 75% quantiles of $\Delta PSNR_{\varphi}(k,l,m)$ distributions, respectively. Dotted lines marks maximal and minimal values of $\Delta PSNR_{\varphi}$ for each algorithm. The horizontal line inside of the box (red in color images) is the median value of these $\Delta PSNR_{\varphi}$.

Let us analyze the results shown in Fig. 4. It is well seen that ImRe-BM3D IT provides the maximal values for $PSNR_{\varphi}$ in majority of the experiments. The box in this box-plot is very narrow, just a horizontal line, and the minimum values of $\Delta PSNR_{\varphi}$ is not much below the box. Thus, the results are very compact and close to the best possible value. ImRe-BM3D IT is outperforming ImRe-BM3D WI in average on 2 dB (in some cases up to 3 dB) and outperforming ImRe-BM3D HT also in average on 2 dB (in some cases up to 7 dB). The advantage of ImRe-BM3D IT with respect to other algorithms even more valuable. Methods WFT, SpInPhase and SPAR are below than ImRe-BM3D IT of about on

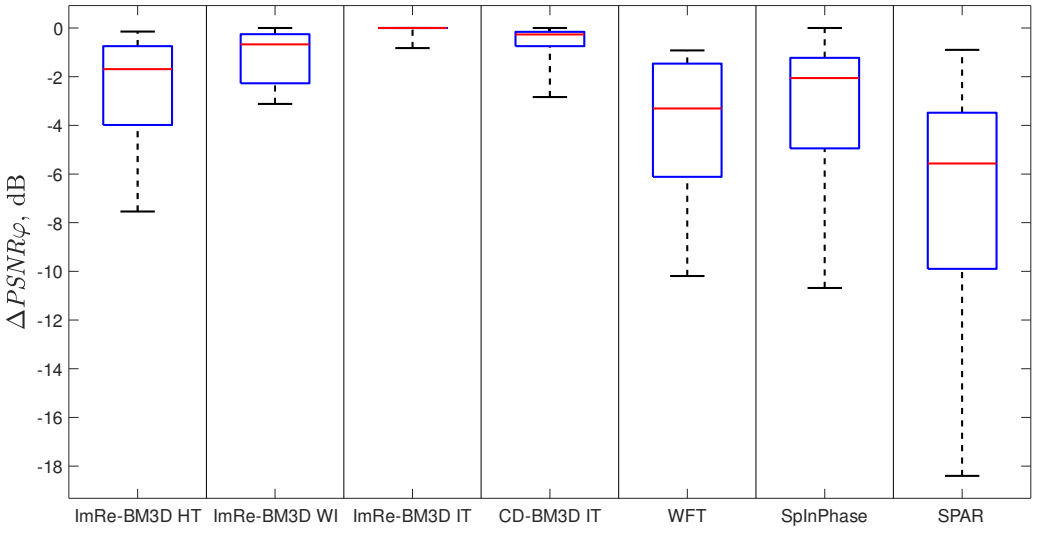

Figure 4. *Box-plots of $\Delta PSNR_\varphi$ for compared algorithms*

2-5 dB and in some cases more than on 10 dB.

In Fig. 5, we can see the results for the Lena test-image, $\sigma_\varphi = .3$. In this case ImRe-BM3D IT outperforms giving the second place SpInPhase more then on 1 dB and provides cleaner and sharper filtered image.

Fig. 9 shows $PSNR_\varphi$ as a function of σ_φ. These curves are calculated as average over the six test-images. It is clearly seen that ImRe-BM3D IT provides always better accuracy with the advance about 2-3 dB.

An example of 3D visualization of comparative performance of SpInPhase and ImRe-BM3D for filtering for absolute phase estimation can be seen in Fig. 7. ImRe-BM3D demonstrates a quite good noise suppression for homogeneous regions outperforming SpInPhase, the closest competitor for the case, more than on 7 dB.

Conclusion

In the paper, the novel iterative complex-valued image denoising algorithms based on HOSVD are proposed as well as the Matlab research toolbox that allows flexible switches between different methods and algorithms. The novel advanced iterative algorithms are proposed. It is shown that they provide the accuracy of about 1 dB better than the current state-of-the-art as well as the other algorithms of in the toolbox.

The proposed MATLAB CDID toolbox for complex-domain (phase/amplitude) denoising is publicly available on http://www.cs.tut.fi/sgn/imaging/sparse/cdid.zip.

Acknowledgement

This work is supported by the Academy of Finland, project no. 138207, 2015-2019.

References

[1] T. Kreis, Handbook of holographic interferometry: optical and digital methods, John Wiley & Sons, 2006.

[2] Q. Kemao, Windowed Fringe Pattern Analysis, SPIE Press Bellingham, Wash, USA, 2013.

[3] K. Dabov, A. Foi, V. Katkovnik, K. Egiazarian, Image denoising by sparse 3-D transform-domain collaborative filtering, IEEE Transactions on image processing 16 (8) (2007) 2080–2095.

[4] V. Katkovnik, K. Egiazarian, J. Bioucas-Dias, Phase imaging via sparse coding in the complex domain based on high-order svd and nonlocal bm3d techniques, in: Image Processing (ICIP), 2014 IEEE International Conference on, IEEE, 2014, pp. 4587–4591.

[5] V. Katkovnik, K. Egiazarian, Sparse phase imaging based on complex domain nonlocal bm3d techniques, Digital Signal Processing 63 (2017) 72–85.

[6] V. Katkovnik, M. Ponomarenko, K. Egiazarian, Sparse approximations in complex domain based on bm3d modeling, Signal Processing (2017) 96–108.

[7] L. R. Tucker, Some mathematical notes on three-mode factor analysis, Psychometrika 31 (3) (1966) 279–311.

[8] J. M. Bioucas-Dias, G. Valadao, Phase unwrapping via graph cuts, IEEE Transactions on Image processing 16 (3) (2007) 698–709.

[9] H. Hongxing, J. M. Bioucas-Dias, V. Katkovnik, Interferometric phase image estimation via sparse coding in the complex domain, IEEE Transactions on Geoscience and Remote Sensing 53 (5) (2015) 2587–2602.

[10] Q. Kemao, Two-dimensional windowed fourier transform for fringe pattern analysis: principles, applications and implementations, Optics and Lasers in Engineering 45 (2) (2007) 304–317.

[11] V. Katkovnik, J. Astola, High-accuracy wave field reconstruction: decoupled inverse imaging with sparse modeling of phase and amplitude, JOSA A 29 (1) (2012) 44–54.

[12] V. Katkovnik, J. Astola, Sparse ptychographical coherent diffractive imaging from noisy measurements, JOSA A 30 (3) (2013) 367–379.

[13] V. Katkovnik, J. Astola, Compressive sensing computational ghost imaging, JOSA A 29 (8) (2012) 1556–1567.

Noisy image, $PSNR_{\varphi}$=25.1 dB ImRe-BM3D IT, $PSNR_{\varphi}$=38.1 dB SpInPhase, $PSNR_{\varphi}$=37.0 dB

Figure 5. *Denoising of test-image lena, σ_{φ}=0.3*

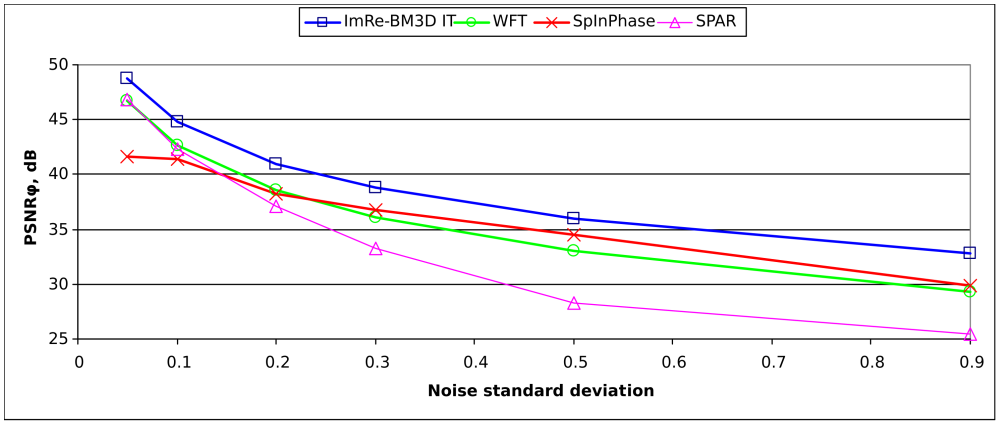

Figure 6. *Averaged $PSNR_{\varphi}$ for interferometric phases*

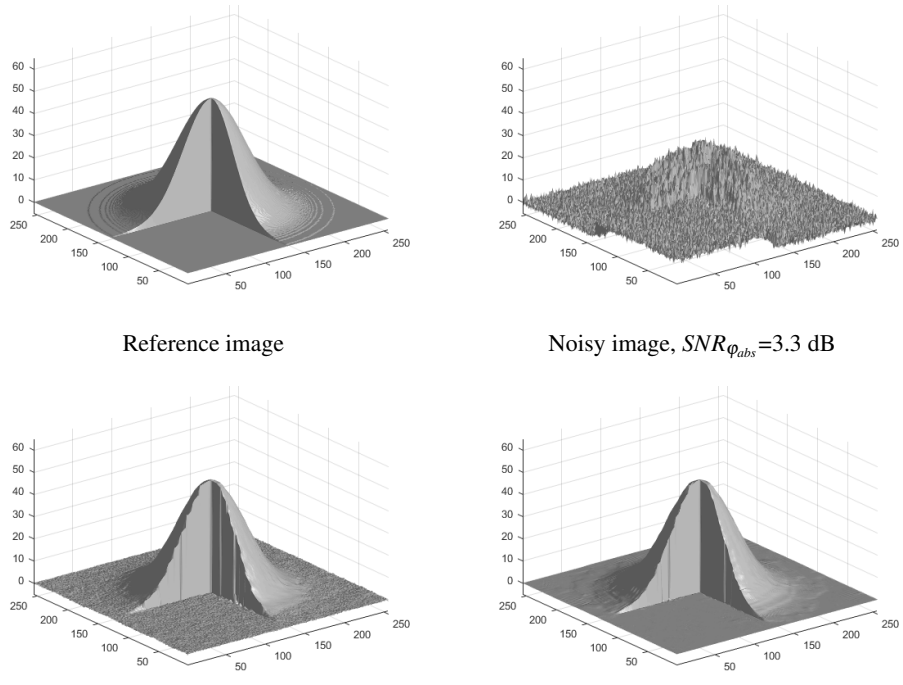

Reference image Noisy image, $SNR_{\varphi_{abs}}$=3.3 dB

SpInPhase, $SNR_{\varphi_{abs}}$=19.4 dB ImRe-BM3D IT, $SNR_{\varphi_{abs}}$=27.0 dB

Figure 7. *Results of absolute phase reconstruction for Truncated Gauss, σ_{φ}=0.9*